International Journal of Heat and Mass Transfer 52 (2009) 1897–1912

Contents lists available at ScienceDirect

International Journal of Heat and Mass Transfer

journal homepage: www.elsevier.com/locate/ijhmt

Effect of thermal buoyancy on vortex shedding past a circular cylinder in cross-flow at low Reynolds numbers

G. Biswas *, Sandip Sarkar

Department of Mechanical Engineering, Indian Institute of Technology – Kanpur, Kanpur 208 016, India

ARTICLE INFO

Article history:
Received 27 February 2008
Received in revised form 14 August 2008
Available online 7 December 2008

ABSTRACT

This paper demonstrates the vortex shedding process behind a heated cylinder in a cross-flow at low Reynolds numbers under the influence of thermal buoyancy. The simulations were performed using an SUPG-based finite element technique. The range of Reynolds numbers was chosen to be 10–45. The flow was steady in the absence of thermal buoyancy. The eddy length and the separation angle were computed for the steady separated flow in the above range of Reynolds numbers. The results were in agreement with those reported in the literature. The Nusselt number distribution around the heated cylinder was also computed in the above range of Reynolds numbers for forced convective flows. The results compared fairly well with available experimental results. The effect of superimposed thermal buoyancy in the same range of Reynolds numbers was studied for various Richardson numbers. The steady separated flows become unsteady periodic in the presence of superimposed thermal buoyancy. For the unsteady periodic flows, the Strouhal numbers were computed. The separation angles and average Nusselt number for such unsteady flows were found to vary with time.

1. Introduction

The structure of the wakes behind bluff obstacles placed in a channel at low Reynolds numbers has been a subject of considerable interest for several decades. The flow over a circular cylinder has wide engineering relevance in various applications, such as heat exchanger tubes, chimney stacks, cooling towers and offshore structures. The most striking phenomenon during the flow past a circular cylinder is vortex shedding. It happens when even a single string or cylinder faces a flow of air or water. The Aeolian harp produces tones when wind blows through it and the chimneys oscillate in a breeze. The knowledge of heat transfer in the wake plays a major role in the development of instruments using wires, such as thermo elements and hot wire anemometers. The influence of thermal buoyancy on the otherwise symmetric wake leads to vortex shedding. The thermal buoyancy plays a role of paramount importance on determining the wake behavior. A notable feature of the superimposed thermal buoyancy is the induced oscillations in the flow field leading to periodic variation of the spatial distribution of Nusselt number on the solid surface. The wake structure is perturbed and the hydrodynamic instabilities grow even at small Reynolds numbers when the wake is severely influenced by thermal or solutal buoyancy. The change in wake length and separation angle with a certain range of Reynolds numbers has been determined by many researchers, both experimentally and numerically (see [1,2]).

Temperature field and heat transfer under forced convection over a circular cylinder up to Reynolds number of 40 was studied by Dennis et al. [3], Jafroudi and Yang [4] and Apelt and Ledwich [5]. Oosthuizen and Madan [6] experimented with mixed convection effects in the range $100 \leq Re \leq 300$. Badr [7] studied numerically laminar mixed convection heat transfer by considering the flow direction both vertically upwards and downwards. Patnaik et al. [8] studied laminar mixed convection heat transfer over single and double cylinders by finite element simulation. Their work alludes to the fact that the naturally occurring Karman Vortex Street degenerates into a twined eddy pattern in the Reynolds number range 41–200 under buoyancy-aided convection. Under buoyancy-opposed convection, they found vortex shedding and formation of twin eddies in a low Reynolds number range of 20–40. Singh et al. [9] simulated mixed convective flow past a cylinder in a vertical channel and found that at a Richardson number of 0.15 or more the shedding is stopped, leading to a situation of twin vortices attached to a cylinder. Biswas et al. [10] studied unsteady mixed convection heat transfer in a horizontal channel with a built-in square obstacle. Their results show that the mixed convection can initiate periodicity and asymmetry in the wake at lower Reynolds numbers, in contrast to forced convection alone. Wang et al. [11] performed experimental investigations on laminar vortex shedding for the flow around a heated cylinder. They derived a new relationship between the wake frequency and the effective Reynolds number. The separation angles for the flow behind a

* Corresponding author. Tel.: +91 512 2597656; fax: +91 512 2597408.
E-mail address: gtm@iitk.ac.in (G. Biswas).

0017-9310/$ - see front matter © 2008 Elsevier Ltd. All rights reserved.
doi:10.1016/j.ijheatmasstransfer.2008.08.034

Nomenclature

D	cylinder diameter
f	vortex shedding frequency
g	acceleration due to gravity
h	heat transfer coefficient
Gr	Grashof number $\left[=\left(\frac{g\beta(T_w-T_\infty)D^3}{\nu^2}\right)\right]$
L_s	eddy length
n_e	total number of elements
N_i, N_m	trial (also called shape/basis) functions
Nu_θ	local Nusselt number on the cylinder surface
$\overline{\mathrm{Nu}_\theta}$	average Nusselt number over the cylinder surface
p	non-dimensional pressure
Pr	Prandtl number $(=\frac{\nu}{\alpha})$
Re	Reynolds number $(=\frac{\rho U_\infty D}{\mu})$
Ri	Richardson number $(=\frac{\mathrm{Gr}}{\mathrm{Re}^2})$
t	non-dimensional time
T	temperature
u, v	non-dimensional velocity components in x and y directions
U_∞	inlet velocity
$\overline{W}$	discontinuous weighting function for SUPG [Eq. (11)]
W	continuous weighting function
$W_{\mathrm{sup\,g}}$	discontinuous streamline upwind contribution of weighting functions
W^h	finite element approximation to test function W
x, y	non-dimensional coordinates

Greek

α	thermal diffusivity of a fluid
β	thermal expansion coefficient
μ	viscosity of a fluid
ρ	density of a fluid
Θ	non-dimensional temperature, i.e. $\left(\frac{T-T_\infty}{T_w-T_\infty}\right)$
τ	time period for a complete cycle
ν	kinematic viscosity of the fluid
θ	angular location on the cylinder surface from the forward stagnation point
θ_s	separation angle
ω	vorticity
$\otimes$	quantity following the symbol is independent of integrating variables

Subscripts

∞	inlet condition
w	wall

Superscripts

e	element
h	finite element approximations of a functions

cylinder up to a Reynolds number of 280 were determined by Wu et al. [12]. They developed an empirical relationship between the separation angle and the Reynolds number in the range $7 \leq \mathrm{Re} \leq 200$. They also determined the effect of blockage on the separation angle. Shi et al. [13] investigated the heating effect on the flow and heat transfer in a two-dimensional laminar flow past a circular cylinder. They considered the variation of fluid properties with temperature in the range $0.001 \leq \mathrm{Re} \leq 170$. They further interpreted the effect of various overheat ratios on the vortex shedding frequency. Kieft et al. [14] analyzed the vortex shedding process for the flow past a circular cylinder for a Reynolds number of 75 and a Grashof number range between 0 and 5000. They showed that the vortices shed from the upper half of the cylinder are stronger than those from the lower half.

In the present investigation, we simulated the flow and heat transfer past a circular cylinder at a blockage ratio $D/H = 0.05$ for the range $10 \leq \mathrm{Re} \leq 45$. The effect of thermal buoyancy was brought about by the varying Richardson number. For the computational work, we introduced a segregated method of solution for the incompressible Navier–Stokes and energy equations using a SUPG (Streamline Upwind Petrov–Galerkin) based finite element method (Maji and Biswas [15]). The algorithm is based on a predictor–corrector approach that uses equal order interpolation functions for velocity, pressure and temperature. The combined effects of forced and natural convection were investigated. Local Nusselt number distributions and isotherms were plotted under forced convection for aforesaid range of Reynolds numbers and compared with the results of Badr [7] and Dennis et al. [3].

2. Governing equations and solution methodology

The incompressible Navier–Stokes and energy equations in the Cartesian coordinate system form the governing equations of the flow. The buoyancy-driven flow from the heated surface interacts with the laminar main flow to yield mixed convection conditions. The dimensionless equations for continuity, momentum and energy with the Boussinesq approximation may be expressed in the following form:

$$\frac{\partial u}{\partial x}+\frac{\partial v}{\partial y}=0 \tag{1}$$

$$\frac{\partial u}{\partial t}+u\frac{\partial u}{\partial x}+v\frac{\partial u}{\partial y}=-\frac{\partial p}{\partial x}+\frac{1}{\mathrm{Re}}\left(\frac{\partial^2 u}{\partial x^2}+\frac{\partial^2 u}{\partial y^2}\right) \tag{2}$$

$$\frac{\partial v}{\partial t}+u\frac{\partial v}{\partial x}+v\frac{\partial v}{\partial y}=-\frac{\partial p}{\partial y}+\frac{1}{\mathrm{Re}}\left(\frac{\partial^2 v}{\partial x^2}+\frac{\partial^2 v}{\partial y^2}\right)+\mathrm{Ri}(\Theta) \tag{3}$$

$$\frac{\partial \Theta}{\partial t}+u\frac{\partial \Theta}{\partial x}+v\frac{\partial \Theta}{\partial y}=\frac{1}{(\mathrm{Re.Pr})}\left(\frac{\partial^2 \Theta}{\partial x^2}+\frac{\partial^2 \Theta}{\partial y^2}\right) \tag{4}$$

where $\mathrm{Re}=\frac{\rho U_\infty D}{\mu}$ is the Reynolds number, $\mathrm{Ri}=\frac{g\beta\Delta\Theta D}{U_\infty^2}=\frac{\mathrm{Gr}}{\mathrm{Re}^2}$ is the Richardson number, g *is* the acceleration due to gravity, Gr is the Grashoff number and $\mathrm{Pr}=\frac{\nu}{\alpha}$ is the Prandtl number; which is taken as 0.7 for the present computations. The fluid properties are described by the thermal diffusivity α, the kinematic viscosity ν and the thermal expansion coefficient β. As to symbols, D is the length scale and U_∞ is the velocity scale of the problem under consideration. Conforming to a blockage ratio of 0.05, the corresponding distance between the top and bottom boundaries is $20D$. Fig. 1 shows the computational domain used in this investigation.

At the inlet, which is located at $X_u = 10D$ upstream of the center of the cylinder, a uniform flow was prescribed ($u = 1, v = 0, \Theta = 0$). At the outlet, which is located at $X_d = 15D$ downstream of the center of the cylinder a homogeneous Neumann boundary conditions for the velocity components (u and v) and temperature (Θ) were used. No-slip conditions were prescribed on the cylinder. At the cylinder surface, uniform temperature ($\Theta = 1$) was prescribed. At the upper and lower confining walls, symmetry conditions simulating a frictionless wall ($\partial u/\partial y = v = 0$) and zero heat flux ($\partial\Theta/\partial y = 0$) were used. The normal derivative of pressure was set to zero on all boundaries except at the outlet where pressure equals the local ambience and hence the Dirichlet condition was set.

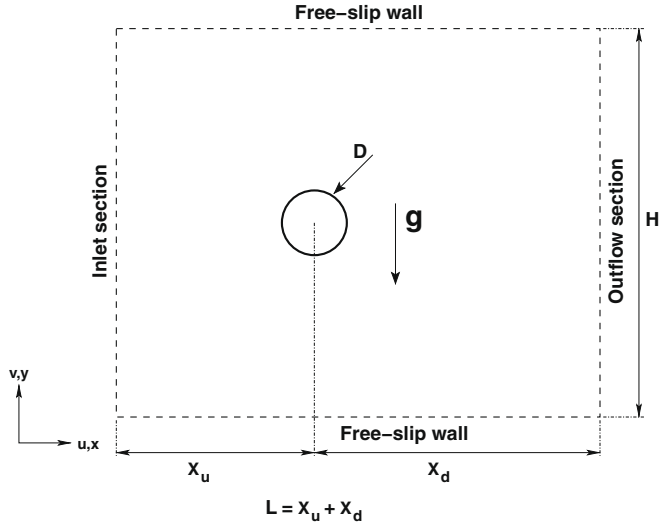

Fig. 1. Physical domain of interest with boundary conditions.

2.1. Solution methodology

To solve the governing equations numerically, a stable finite element method was used. The Eulerian velocity correction approach based on the Projection scheme identical with the Marker and Cell (MAC) method of Harlow and Welch [16] was used to solve the governing equations for the mass, momentum and energy. An explicit time-stepping numerical technique with the Streamline Upwind Petrov–Galerkin (SUPG) formulation (Brooks and Hughes [17]) was adopted. This present work is an extension of the earlier work of Maji and Biswas [15]. The method has been successfully applied to solve complex problems (Prakash et al. [18]; Kumar and Biswas [19]).

2.2. Finite element formulation

Eqs. (2) and (3) without the pressure term and Eq. (4) may be represented as a single equation:

$$\frac{\partial \Phi}{\partial t} + u\frac{\partial \Phi}{\partial x} + v\frac{\partial \Phi}{\partial y} = \frac{1}{\wp}\left(\frac{\partial^2 \Phi}{\partial x^2} + \frac{\partial^2 \Phi}{\partial y^2}\right) + S_\Phi \tag{5}$$

where $\Phi = \{u, v, \Theta\}$ and S_Φ is the source term, which is zero except for the y-momentum equation. The term $\wp$ represents Re and RePr for momentum and energy equations, respectively.

Let Ω (geometry of interest) be a bounded region in $\Re^2$ bounded by the piecewise smooth boundary Γ. Let $\boldsymbol{x} = \{x, y\}$ denote the vector of spatial coordinate of a generic point in $\overline{\Omega}$ and let t denote the time value in the interval $I = [0, T]$. Let $\overrightarrow{n}$ be the outward normal vector to Γ and Γ_g, Γ_h as sections of Γ which satisfy the following:

$$\overline{\Gamma_g \cup \Gamma_h} = \Gamma \tag{6}$$

$$\Gamma_g \cap \Gamma_h = \varnothing \tag{7}$$

The over-bar in Eq. (6) represents set closure and $\varnothing$ in Eq. (7) denotes an empty set. In order to find a discrete solution of the governing equations, we assume Ω is discretized into n_e quadrilateral elements such that

$$\bigcup_{e=1}^{n_e} \overline{\Omega^e} = \overline{\Omega} \qquad \bigcap_{e=1}^{n_e} \overline{\Omega^e} = \varnothing \tag{8}$$

where Ω^e denotes the interior domain of an element. Let (Φ^h, p^h) be an element of S^h and W^h be an element of V^h, where S^h and V^h are finite dimensional subspaces of the trial (S) and test (V) spaces, respectively, and are defined as

$$S^h = \left\{(\Phi^h) \in (C^0(\Omega))^6, \Phi^h = g_\Phi \quad \text{and} \quad p^h = s \text{ on } \Gamma_g^*\right\}$$

$$V^h = \left\{W^h \in C^0(\Omega), W^h = 0 \text{ on } \Gamma_g^*\right\}$$

where $\Gamma_g^* = \Gamma_g$, when Φ is specified and $\Gamma_g^* = \Gamma_h$ when pressure is specified. g_Φ and s are the Dirichlet boundary values. In the present formulation an equal order interpolation is used for all unknowns. The functions are of Lagrange type that belongs to class $H^1(\Omega)$, i.e. they are $C^0(\Omega)$ continuous. Now the finite element method can be formulated by requiring the discrete solution Φ^h to satisfy the weak form of Eq. (5):

$$\int_\Omega W^h\left[\frac{\partial \Phi^h}{\partial t} + u^h\frac{\partial \Phi^h}{\partial x} + v^h\frac{\partial \Phi^h}{\partial y}\right]d\Omega + \frac{1}{\wp}\int_\Omega\left[\frac{\partial W^h}{\partial x}\frac{\partial \Phi^h}{\partial x} + \frac{\partial W^h}{\partial y}\frac{\partial \Phi^h}{\partial y}\right]d\Omega = \frac{1}{\wp}\int_{\Gamma_h} W^h h_\Phi d\Gamma + \int_\Omega W^h S_\Phi d\Omega \tag{9}$$

where h_Φ is the respective Neuman boundary condition of the momentum and energy equations.

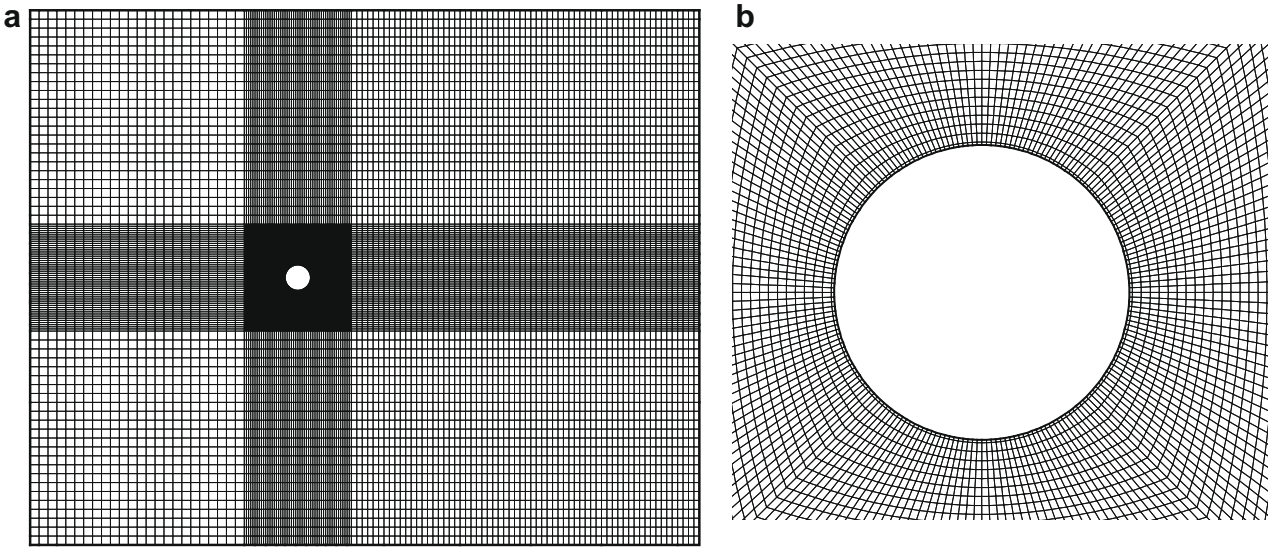

Fig. 2. (a) Typical grid used for computation. (b) A closer view of the grid around the cylinder.

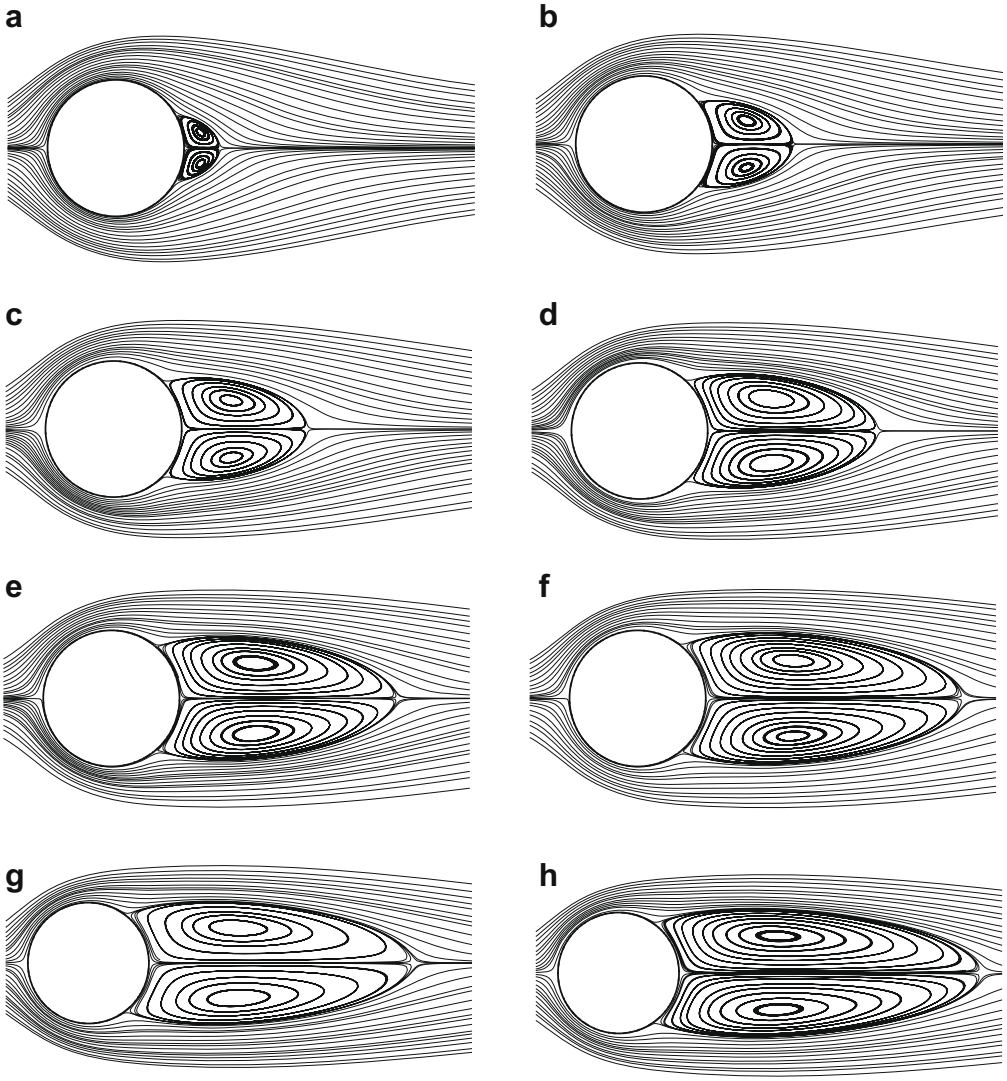

Fig. 3. Streamlines of the flow for Re = (a) 10, (b) 15, (c) 20, (d) 25, (e) 30, (f) 35, (g) 40 and (h) 45.

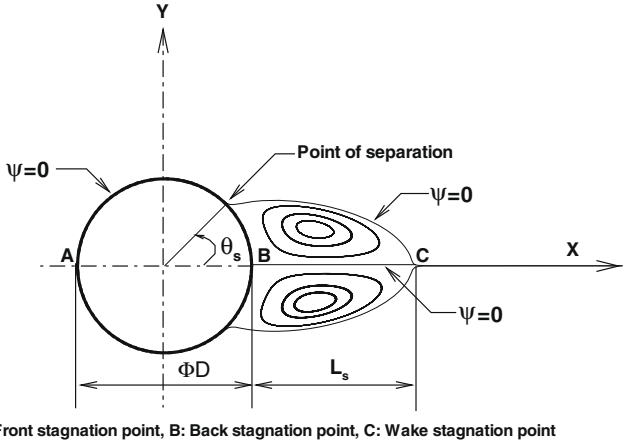

Fig. 4. Schematic of the wake-bubble geometry.

Let the finite set $\{N_i\}$ represent basis functions for S^h and $\{W_i\}$ be the basis functions for V^h. The discrete solution Φ^h can be approximated within each element as a linear combination of the trial (basis) function. The expression for Φ^h is given as

Table 1
Comparison of L_s values at Re values of 10–45.

Re	Present calculation	Takami and Keller [20]	Dennis and Chang [21]
10	0.521	0.500	0.53
15	1.189	1.162	–
20	1.865	1.844	1.88
25	2.517	–	–
30	3.226	3.223	–
35	3.793	–	–
40	4.424	4.650	4.69
45	5.033	–	–

Table 2
Comparison of θ_s values at Re values of 10–45.

Re	Present calculation	Takami and Keller [20]	Dennis and Chang [21]
10	29.12	29.3	29.6
15	38.57	38.6	–
20	43.64	43.65	43.7
25	46.89	–	–
30	49.29	49.6	–
35	51.35	–	–
40	53.10	53.55	53.8
45	54.56	–	–

$$\Phi^{h} = \sum_{m=1}^{N_p} \left\{ \Phi(t) \right\}_m N_m = \{N\}^T \{\Phi(t)\} \right\} \tag{10}$$

where N_p is the total number of nodes in each element. The formulation has been documented in the work of Prakash et al. [18] and Kumar and Biswas [19].

2.3. Streamline Upwind Petrov–Galerkin formulation

The numerical scheme based on standard Bubnov–Galerkin finite element method (GFEM) for convection–diffusion problems produces a non-physical oscillatory solution when convection dominates over diffusion. To overcome this problem, Brooks and Hughes [17] introduced the Streamline Upwind Petrov–Galerkin (SUPG) technique with the application of modified weighting functions for all terms of the governing equations given by

$$\overline{W^h} = W^h + W^{gh}_{sup} \tag{11}$$

where W^h is a continuous weighting function and W^h_{supg} is the discontinuous streamline upwind contribution. Both W^h and W^h_{supg} are assumed to be smooth on the element interiors. The above discontinuous test functions W^h_{supg} introduce a corrective diffusion which is highly anisotropic with a non-zero coefficient only in the direction of the resultant element velocity vector calculated at the geometric center of the element. This is to make this term active only in the direction of the resultant element velocity and thereby effectively introduces upwinding in a multi-dimensional problem. It should be noted that in the SUPG formulation, W^h_{supg} weights only in the element interiors. Also, the element coefficient matrix is mass lumped. Incorporating all these concepts, Eq. (9) may be rewritten as

$$\begin{aligned}
&\sum_{e=1}^{n_e} \int_{\Omega^e} [\overline{W}] d\Omega \otimes \left\{ \frac{\Phi^* - \Phi^n}{\Delta t} \right\} \\
&\quad \approx -\sum_{e=1}^{n_e} \int_{\Omega^e} \{\overline{W}\} \left[\{N\}^T \{u^n\} \left\{ \frac{\partial N}{\partial x} \right\}^T \{\Phi^n\} \right. \\
&\quad \left. + \{N\}^T \{v^n\} \left\{ \frac{\partial N}{\partial y} \right\}^T \{\Phi^n\} \right] d\Omega + \sum_{l} \int_{\Gamma^l_h} \{W\} \left(\frac{1}{\wp} \right) h_\phi d\Gamma \\
&\quad - \sum_{e=1}^{n_e} \int_{\Omega^e} \left(\frac{1}{\wp} \right) \left[\left\{ \frac{\partial W}{\partial x} \right\} \left\{ \frac{\partial N}{\partial x} \right\}^T \{\Phi^n\} + \left\{ \frac{\partial W}{\partial y} \right\} \left\{ \frac{\partial N}{\partial y} \right\}^T \{\Phi^n\} \right] d\Omega \\
&\quad + \sum_{e=1}^{n_e} \int_{\Omega^e} \{\overline{W}\} S^h_\phi d\Omega
\end{aligned} \tag{12}$$

where n_e is the total number of elements in the domain Ω. Eq. (12) allows us to compute the provisional value Φ at the new time step in terms of the quantities at the previous time step value.

3. Grid generation and code validation

The computational domain is discretized into small curvilinear four-noded elements. The grid is generated based on the multi-

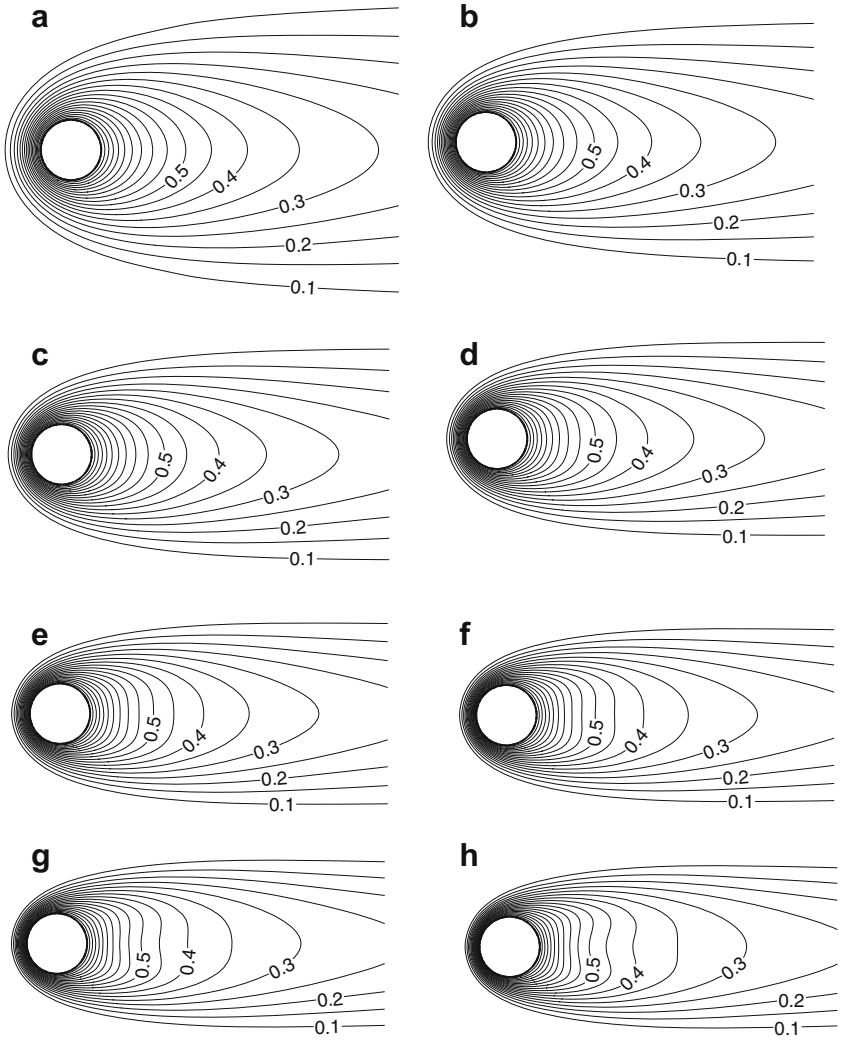

Fig. 5. Temperature contours of the flow for Re = (a) 10, (b) 15, (c) 20, (d) 25, (e) 30, (f) 35, (g) 40 and (h) 45.

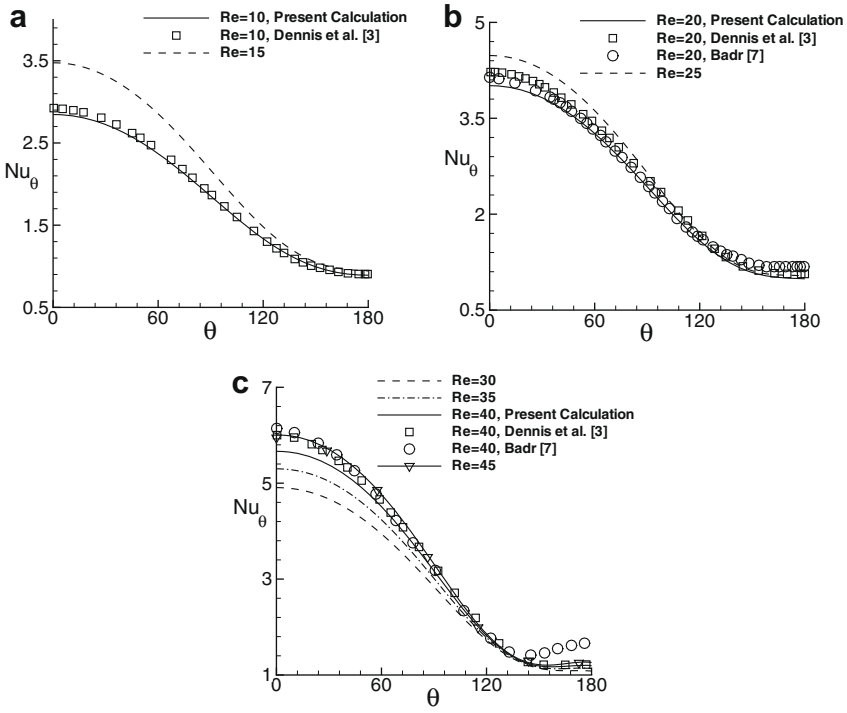

Fig. 6. Variation of local Nusselt number on the cylinder surface for Re = (a) 10 and 15, (b) 20 and 25, (c) 30, 35, 40 and 45.

block technique using the transfinite interpolation (algebraic method) further smoothed by a partial differential equation of elliptic type. The velocity components, pressure and temperature are collocated at each node of the element. A typical grid is shown in Fig. 2(a). The grid is refined very fine around the cylinder [Fig. 2(b)] and made a little coarse in the far field.

This SUPG-based finite element code has been tested satisfactorily on a number of benchmark problems, such as the flow in a lid-driven cavity, the flow over a backward-facing step and the flow in a buoyancy-driven cavity. The results are presented elsewhere [18] and they are found satisfactory. In the present investigation, the algorithm was applied to a dynamic problem and results were verified. For a blockage of 0.05, computations were made with 17,952, 21,024 and 24,252 quadrilateral elements and 18,264, 21,360 and 24,614 nodes, respectively. The grid-independent situation was achieved for 21,024 quadrilateral elements and 21,360 nodes.

Biswas et al. [10] investigated the influence of superimposed thermal bouncy in a horizontal channel with built-in square cylinder. When the flow velocity is not very high and the temperature difference between the body and the ambient fluid is large, the flow characteristics are strongly influenced by the thermal buoyancy. Their results showed that the buoyancy can initiate periodicity and asymmetry in the wake at low Reynolds numbers for a blockage 0.25. Therefore the influence of superimposed thermal buoyancy on the bluff body wake is well understood for the higher blockage. It is needed to investigate the flows using a lower blockage in order to reduce the influence of confining surfaces. In the present investigation we have used a blockage of 0.05 and it is close to flow in infinite medium [2].

4. Results and discussion

4.1. Flow and heat transfer characteristics under forced convection

The finite element simulations were carried out for a range of Reynolds number from 10 to 45. Results were obtained corresponding to steady-state conditions. The wake structures were studied from the streamlines plots. Fig. 3(a)–(h) show the streamlines for Reynolds numbers of 10, 15, 20, 25, 30, 35, 40 and 45.

The usual features of the flow field are revealed from these plots. These features are the reflection symmetry of streamlines about the centerline of the flow and the steady growth of the recirculation zone with the Reynolds number. Here, the important parameters of interest are the eddy length and the separation angle. Fig. 4 shows the typical bubble geometry of the flow, where the eddy length L_s and separation angle θ_s have been defined. The length of the eddy is the measure from the rear of the cylinder to the wake stagnation point and the angle of separation is the an-

Table 3
Comparison of $\overline{Nu_\theta}$ values at Re values of 10–45.

Re	Present calculation	Dennis et al. [3]	Jafroudi and Yang [4]	Apelt and Ledwich [5]
10	1.8577	1.897	1.821	1.864
15	2.1809	–	2.176	2.193
20	2.4483	2.557	2.433	–
25	2.6802	–	–	–
30	2.8877	–	2.850	–
35	3.0772	–	–	–
40	3.2531	3.480	3.200	3.255
45	3.4178	–	–	–

Table 4
Reynolds numbers (Re) and the corresponding Richardson numbers (Ri) and Strouhal numbers (St) signifying the onset of vortex shedding.

Re	Ri	St
10	1.400	0.05037
15	1.750	0.05750
20	1.750	0.05873
25	1.750	0.05900
30	1.800	0.05990
35	1.850	0.06044
40	1.950	0.06169
45	1.985	0.06197

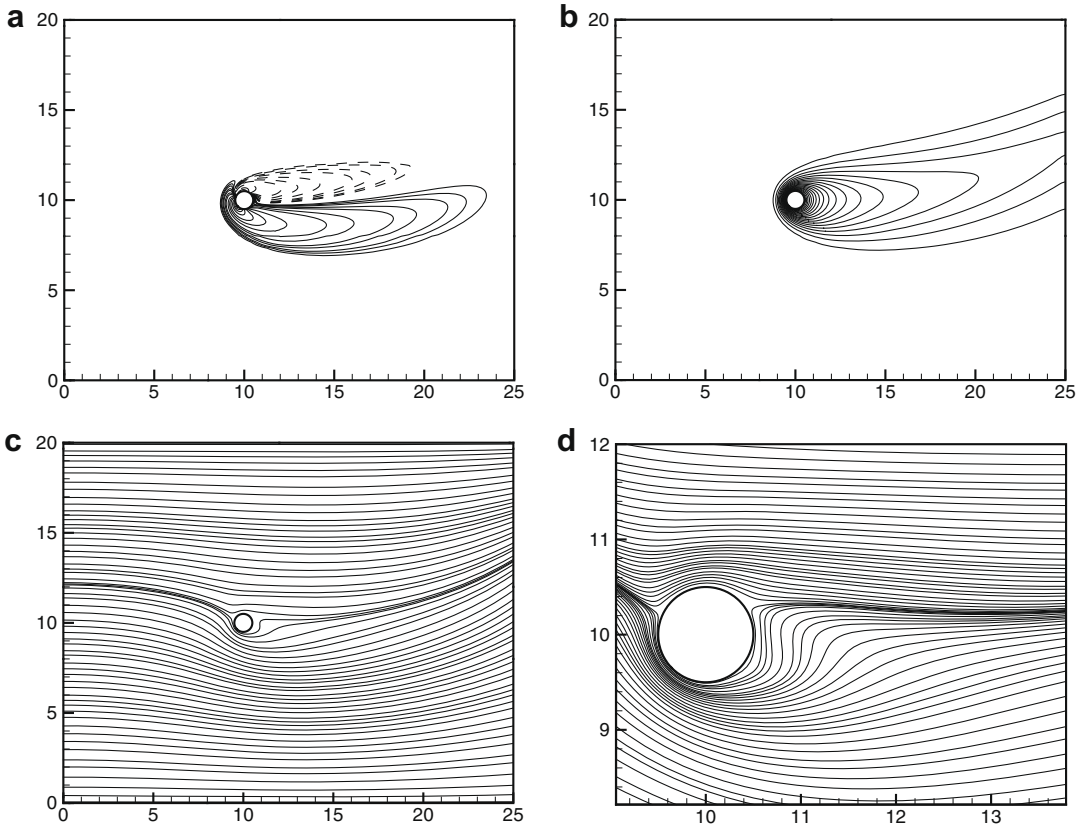

Fig. 7. Behavior of wake at Re = 10 and Ri = 1.0. (a) Contours of ω; (b) isotherms; (c) streamlines; (d) close-up view of streamlines.

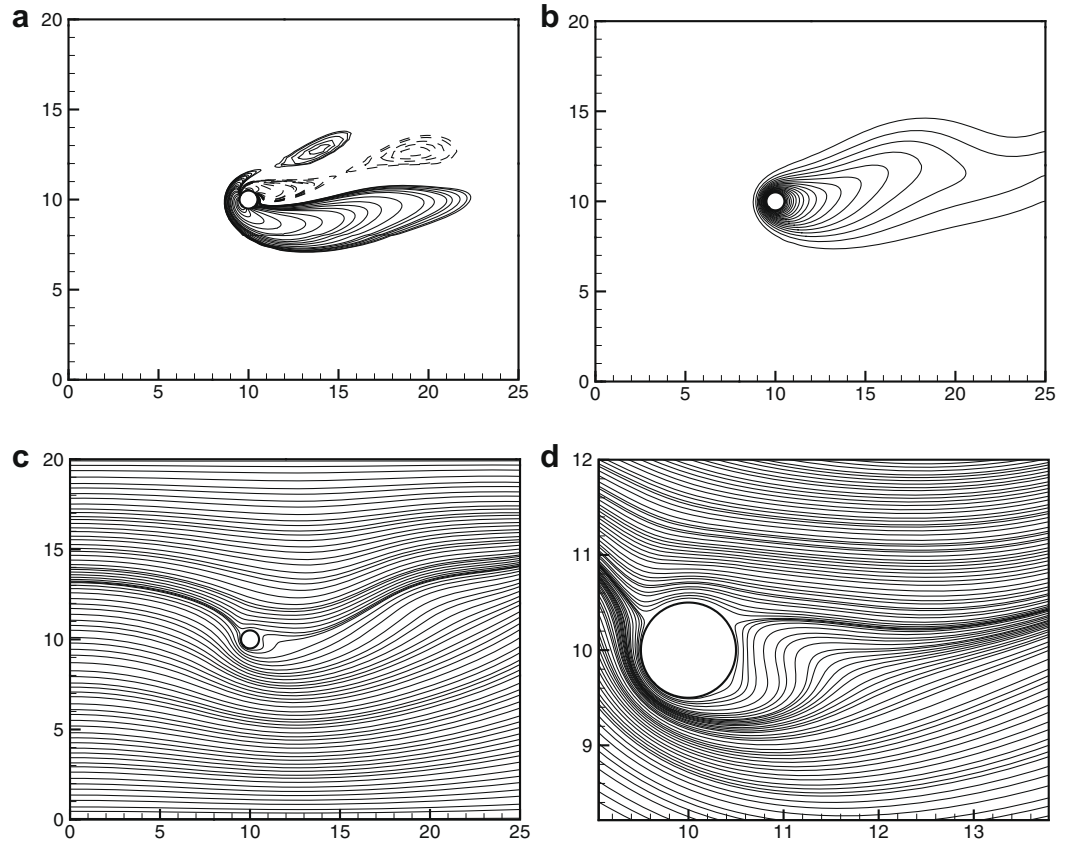

Fig. 8. Behavior of wake at Re = 10 and Ri = 1.5. (a) Contours of ω; (b) isotherms; (c) streamlines; (d) close-up view of streamlines.

gle measured from the rear stagnation point to the point on the cylinder where the vorticity vanishes. The calculated lengths of the eddies and angles of separation for the above-mentioned range of Reynolds numbers were found to be in good agreement with the numerical results of Takami and Keller [20] and are shown in Tables 1 and 2.

It is evident from Table 1 that the eddy length increases linearly with increasing Reynolds number over the range of interest. The present calculations are also in close agreement with the results obtained in other numerical studies by Dennis and Chang [21].

For the case of flow past a heated cylinder, the temperature contours were obtained to investigate the effect of Reynolds number on heat transfer. Fig. 5(a)–(h) show the isotherms around the heated cylinder for Reynolds numbers of 10, 15, 20, 25, 30, 35, 40 and 45. The isotherms appear symmetrical about the line of symmetry in the wake region.

Fig. 5(a)–(h) reveal that temperature contours becomes steeper in the near-wake region with increasing Reynolds number. This means that an increasing Reynolds number, signifying a higher fluid velocity, sets a higher temperature gradient, leading to enhanced heat transfer from the cylinder surface.

The quantitative parameter indicating heat transfer, i.e. the local Nusselt number based on the cylinder diameter, is defined as

$$Nu_\theta = -\frac{\partial \Theta}{\partial n}\bigg|_{\text{along the cylinder surface}} \tag{13}$$

where n denotes the direction normal to the cylinder surface and θ is the polar angle. The location $\theta = 0$ corresponds to the front stagnation point facing the incoming flow.

The local Nusselt number distribution for the present range of Reynolds numbers was calculated and compared with the results of Dennis et al. [3] and Badr [7] and there was good agreement. Fig. 6(a) shows the local Nusselt number distribution over the cylinder surface for the Reynolds numbers of 10 and 15. Similarly Fig. 6(b) shows the local Nusselt number distribution for the Reynolds numbers of 20 and 25. The predicted results due to present computations for the Reynolds number of 20 compare quite well with the investigations of Dennis et al. [3] and Badr [7]. The local Nusselt number distribution over the cylinder surface for the Reynolds numbers of 30, 35, 40 and 45 are summarized in Fig. 6(c). In all the cases, it can be seen that the Nusselt number decreases gradually from the forward stagnation point to the rear stagnation point. This trend of variation supports the fact that maximum heat transfer is brought about at the forward stagnation point and then the heat transfer decreases gradually along the cylinder surface and finally the minimum value is reached at the rear stagnation point. The local Nusselt number at any given θ reveals a higher value for higher Reynolds numbers.

The average Nusselt numbers $\overline{Nu_\theta}$ were calculated for the Reynolds numbers of interest and are given in Table 3. The results of the present simulation show good agreement with the numerical solutions of Dennis et al. [3], Apelt and Ledwich [5] and Jafroudi

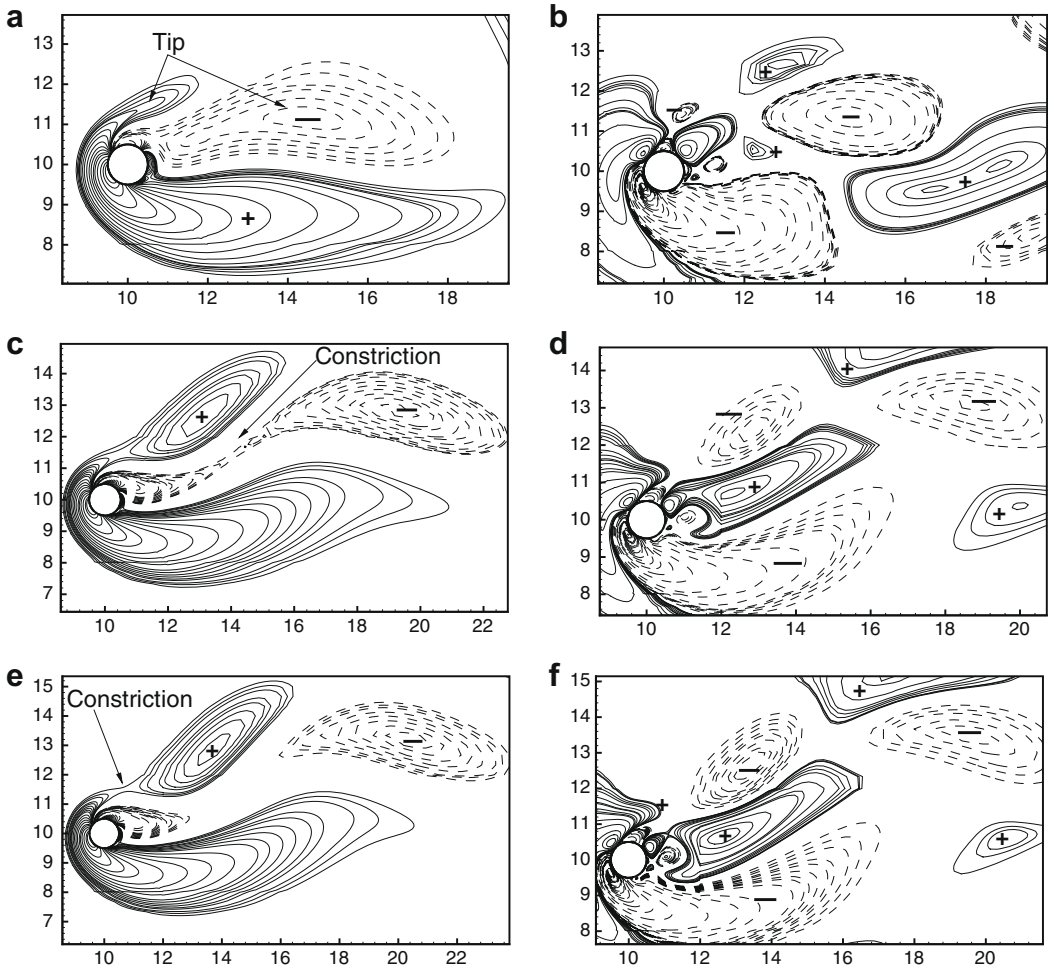

Fig. 9. Instantaneous contours of ω for Re = 10 and Ri = 2.0 at (a) t, (c) $t+\frac{\tau}{3}$, (e) $t+\frac{2\tau}{3}$ (close-up view). Instantaneous contours of γ for Re = 10 and Ri = 2.0 at (b) t, (d) $t+\frac{\tau}{3}$, (f) $t+\frac{2\tau}{3}$ (close-up view).

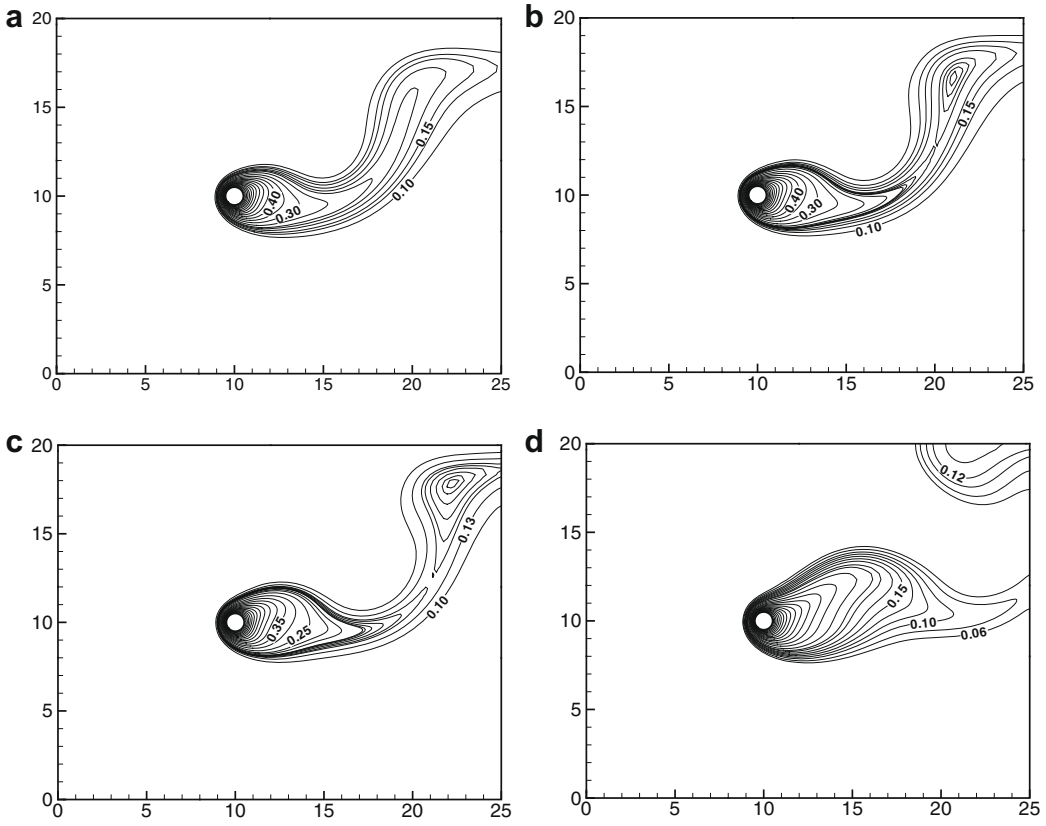

Fig. 10. Instantaneous isotherms of flow for Re = 10 and Ri = 2.0 at (a) t, (b) $t+\frac{\tau}{4}$, (c) $t+\frac{2\tau}{4}$, (d) $t+\frac{3\tau}{4}$.

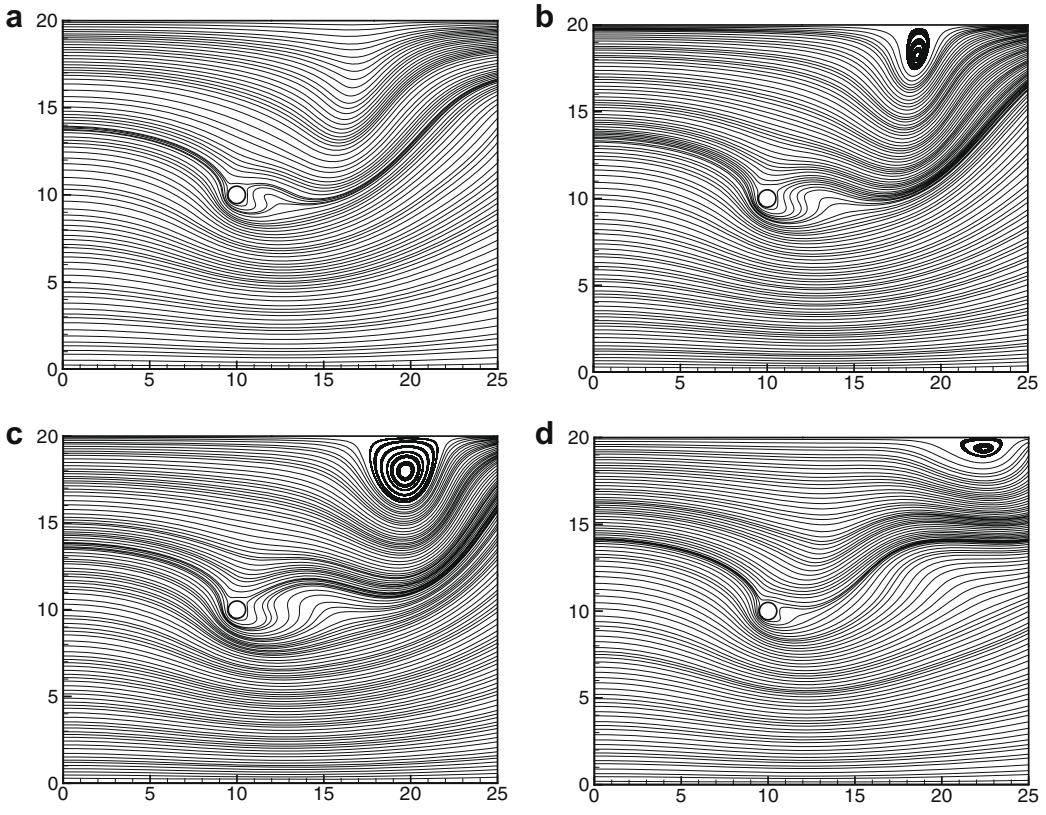

Fig. 11. Instantaneous streamlines of flow for Re = 10 and Ri = 2.0 at (a) t, (b) $t+\frac{\tau}{4}$, (c) $t+\frac{2\tau}{4}$, (d) $t+\frac{3\tau}{4}$.

and Yang [4]. Table 3 shows that the average Nusselt number increases monotonically with increase in Reynolds number.

4.2. Flow and heat transfer characteristics under superimposed buoyancy-induced convection

The parameter that governs the buoyancy-induced effect is indicated by the Richardson number Ri. We studied the situations for $1.0 \leq \mathrm{Ri} \leq 2.0$ and the Reynolds numbers of interest are $10 \leqslant \mathrm{Re} \leqslant 45$. For the above range of Ri, the flow and the wake zone dynamics are significantly influenced by the thermal buoyancy, and vortex shedding is observed. The periodicity is characterized by the frequency of vortex shedding f. The dimensionless vortex shedding frequency is expressed as $\frac{fD}{U_\infty}$, known as the Strouhal number (St). Where D is the diameter of the cylinder and U_∞ is the free stream velocity. Table 4 shows the simulation results for the Richardson numbers at which vortex shedding is first observed for the present range of Reynolds numbers. The corresponding vortex shedding frequencies, expressed as Strouhal numbers, are also given.

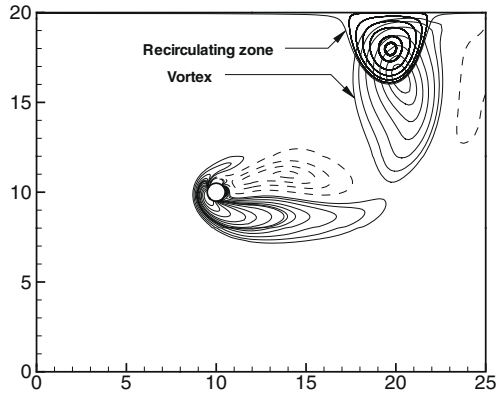

Fig. 12. Instantaneous contours of ω and streamlines during vortex shedding cycle at Re = 10 and Ri = 2.0.

The vortex shedding process is initiated by the formation of a vortex blob at the downstream of the cylinder wake [14]. This formation of a vortex blob occurs by the transportation of vorticity produced in the vicinity of the cylinder surface to the cylinder near wake. Green and Gerrard [22] described the vortex formation process as a sequence of three interconnected stages. During the first stage, the vorticity originating from the boundary layer accumulates and produces a coherent vortex blob at the tip of the strand. During the second stage, the vortex blob separates from the strand. This separation of the vortex blob is brought about by the initiation of a constriction process upstream of the strand tip, which transforms into a region of coherent vortex structure (see Kieft et al. [14]). It is assumed that at a Reynolds number of 10 and a Richardson number of about 1.4, a high shear rate develops in the constriction area and causes this constriction process. The shear rate causes dissipation of kinetic energy in the constriction area. The advection and entrainment initiate this constriction phenomenon (Green and Gerrard [22], Gerrard [23]). In the third and last stage, the detached vortex blob from the constriction area moves downstream of the cylinder and vortex shedding starts. Here we define a parameter γ that describes vorticity accumulation and vortex structure formation (Kieft et al. [14]). The parameter may be expressed as (also see Kieft et al. [24])

$$\gamma = \frac{1}{2}(\sigma_1^2 + \sigma_2^2 - \omega^2) \tag{14}$$

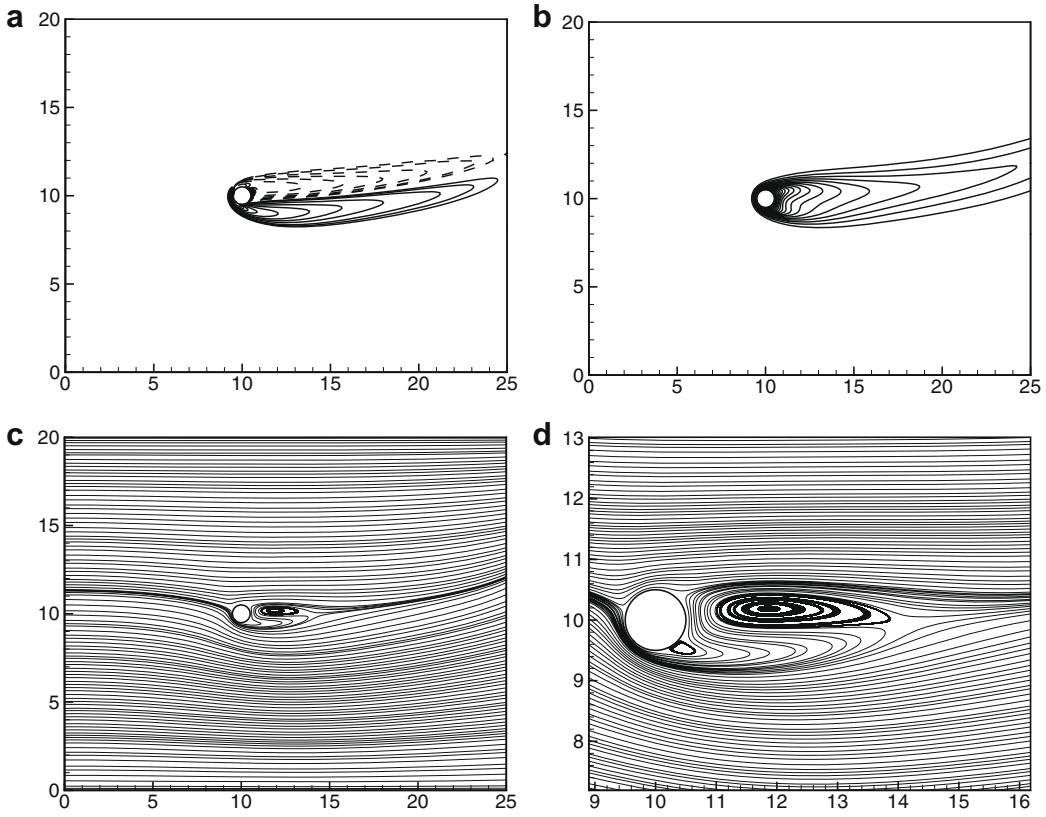

Fig. 13. Behavior of wake at Re = 45 and Ri = 1.0. (a) Contours of ω; (b) isotherms; (c) streamlines; (d) close-up view of streamlines.

where

$$\sigma_2 = \frac{\partial v}{\partial x} + \frac{\partial u}{\partial y} \text{ is the shear rate,}$$

$$\omega = \frac{\partial v}{\partial x} - \frac{\partial u}{\partial y} \text{ is the vorticity} \quad (15)$$

and

$$\sigma_1 = \frac{\partial u}{\partial x} - \frac{\partial v}{\partial y} \quad (16)$$

The quantitative value of γ is calculated. If the quantity γ becomes negative, the motion is said to be elliptical. However, a positive γ corresponds to hyperbolic motion. In fact, Weiss [25] showed that $\gamma < 0$ indicates the elliptic regions signifying accumulation of vorticity with increasing local circulation, whereas $\gamma > 0$ indicates hyperbolic regions signifying stretching of vorticity that prevents the growth of a coherent structure. Therefore in the elliptic regions coherent vortex structures originate and in hyperbolic regions the strain rate is dominant, causing stretching and deformation of fluid elements.

It may be mentioned that the flow field may be described by

$$\mathbf{V} = u\hat{i} + v\hat{j} \quad (17)$$

$$\mathrm{tr}\mathbf{A} = \nabla.\mathbf{V} = \frac{\partial u}{\partial x} + \frac{\partial v}{\partial y} \quad \text{and} \quad \mathbf{A} = \nabla\mathbf{V} \quad (18)$$

The parameter $\mathrm{tr}\mathbf{A}^2$ can be expressed as

$$\mathrm{tr}\mathbf{A}^2 = \frac{1}{2}(\lambda\tilde{\lambda} - \omega^2) \quad (19)$$

$$\lambda = \sigma_1 + i\sigma_2 \quad \text{whereas} \quad \tilde{\lambda} = \sigma_1 - i\sigma_2 \quad (20)$$

$$\lambda\tilde{\lambda} = (\sigma_1 + i\sigma_2)(\sigma_1 - i\sigma_2) = \sigma_1^2 + \sigma_2^2$$

$$\lambda\tilde{\lambda} = \left(\frac{\partial u}{\partial x} - \frac{\partial v}{\partial y}\right)^2 + \left(\frac{\partial v}{\partial x} + \frac{\partial u}{\partial y}\right)^2$$

Therefore

$$\lambda\tilde{\lambda} - \omega^2 = \sigma_1^2 + \sigma_2^2 - \omega^2 \quad (21)$$

Thus γ may also be interpreted as $\mathrm{tr}\mathbf{A}^2$.

In the present investigation, the vortex shedding process under the influence of buoyancy at low Reynolds numbers was analyzed by calculating the contours of both ω and γ. Specifically for Ri = 2.0 and for the same Reynolds number range 10–45, the contours of ω and γ for different time instants were calculated to identify the effect of buoyancy on vortex shedding. Also, the contours of streamlines and temperatures were obtained to visualize the effects of high heating. The results are shown for Re = 10 and Re = 45 and for different values of Ri.

4.3. Behavior of the wake under superimposed buoyancy at Re = 10

Depending on the magnitude of Ri the point of separation moves towards the leading edge, causing an early separation. A steady wake is found below Ri = 1.4 for Re = 10. Fig. 7(a–d) show the steady-state solutions for Ri = 1.0.

From the streamlines plots in Figs. 3(a) and 7(d), it is found that increasing Ri from zero to one results a decrease in the recirculation bubble. A similar phenomenon was also observed by Badr [7].

Figs. 8(a–d) show the behavior of wake for Ri = 1.5 at Re = 10. At this Ri the wake becomes unsteady and vortex shedding is observed. The vortex structure formation process is described in Figs. 9(a–f) for Re = 10 and Ri = 2.0 with the iso-contours of ω and γ computed at the vortex shedding cycle at three different time instants.

The shedding process starts with the generation of an upper vortex blob identified by the stretching of the vorticity strand at the upper cylinder shoulder, which is shown in Fig. 9(a). The tip of the vorticity strand is located at an area where $\gamma < 0$ [Fig. 9(b), at $x/D \approx 15.0$ and $y/D \approx 11.0$]. Within that area, vorticity transported from the boundary layers, produced at the vicinity of the

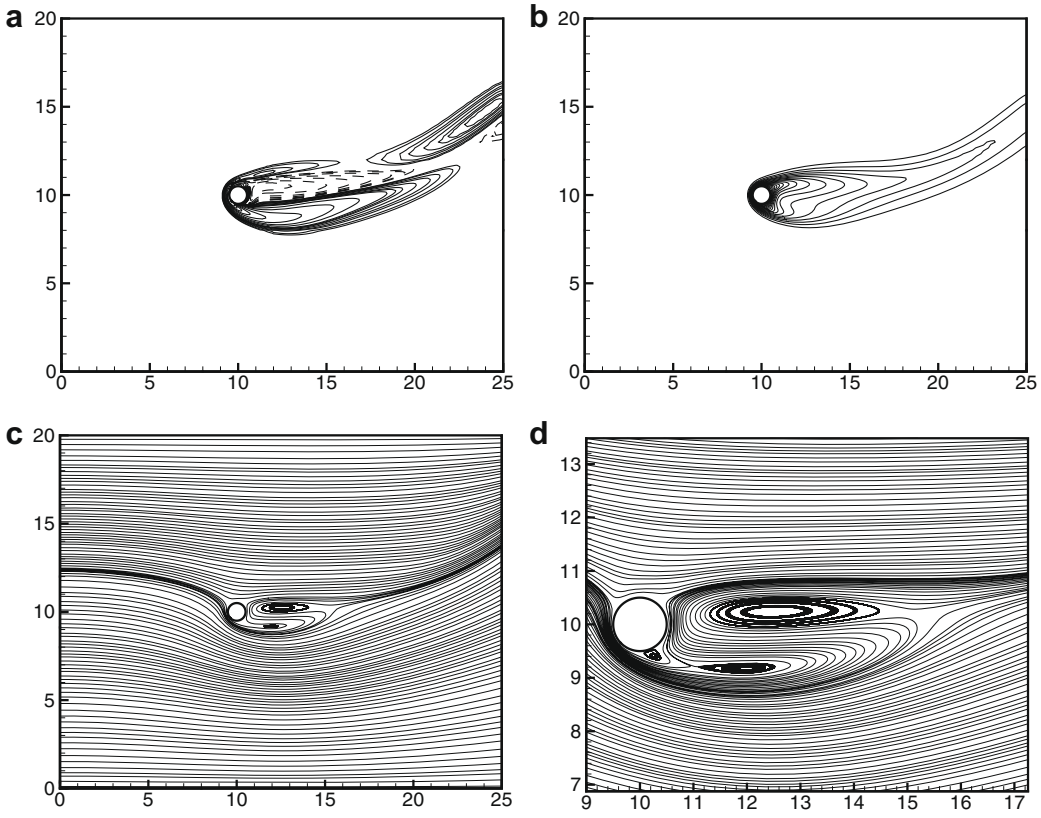

Fig. 14. Behavior of wake at Re = 45 and Ri = 1.985. (a) Contours of ω; (b) isotherms; (c) streamlines; (d) close-up view of streamlines.

cylinder surface, is comparatively unaffected by shear stress and finally leads to the formation of coherent structures. A local vorticity extreme forms at the tip of the vorticity strand having an area of strongly negative γ [Fig. 9(c) and (d), at $x/D \approx 19.0$ and $y/D \approx 13.0$]. The local vorticity extreme grows slowly and is gradually convected in the downstream direction and the vorticity strand that connects the local vorticity extreme with the boundary layer starts to constrict between $x/D \approx 13.0$ and ≈ 15.0 at $y/D \approx 11.0$ and ≈ 12.0 [Fig. 9(c) and (d)]. This constriction of the vorticity strand occurs in an area of $\gamma > 0$, [Fig. 9(d)] indicating a dominant strain rate. In the later stages, the area where $\gamma > 0$ rapidly increases and finally reaches its maximum value. At the instant when the vorticity structure reaches its developed stage, it becomes disconnected from the vorticity strand and moves due advection downstream of the cylinder [Fig. 9(e)].

The shedding of the lower vortex starts one stage later than that of the upper vortex [Fig. 9(e)]. Similarly to the upper vortex, the lower vortex also sheds from the upper half of the cylinder shoulder. This is because of the effect of the high superimposed buoyancy. The lower vorticity strand is stretched to the upper half of cylinder shoulder where its tip is positioned within an area of $\gamma < 0$ [Fig. 9(a) and (b) at $x/D \approx 11.0$ and $y/D \approx 11.5$]. By comparing this area with that found during the generation of an upper vortex [Fig. 9(b), (d) and (f)], the extreme value of γ is found to be very negative for the upper vortex. It is found from the simulations that [Fig. 9(b), (d) and (f)] the size of the area occupied by $\gamma < 0$ is higher for the lower vortex than the upper vortex. This means that the accumulation of vorticities for the formation of a lower vortex blob takes place in a larger area and is highly affected by the strain rate. That is why the local vorticity extreme developed at a later stage during the formation process.

The formation of the shed structures from the upper side of the cylinder differs from the one shed from the lower side. The results show that due to the addition of thermal energy an asymmetry arises between the formation process of an upper and lower vortex. The upper vortices are formed closer to the cylinder compared to the lower ones. The formation process of an upper vortex is less influenced by strain. This finally culminates in the formation of upper vortices which have a higher vorticity extreme and also have a higher temperature. Fig. 9 suggests that while a lower vortex forms and grows in size, due to buoyancy, a new structure with positive vorticity is shed from the upper half region of the cylinder.

With the advection of vorticity, the thermal energy is advected downstream of the cylinder. The geometric difference in the iso-

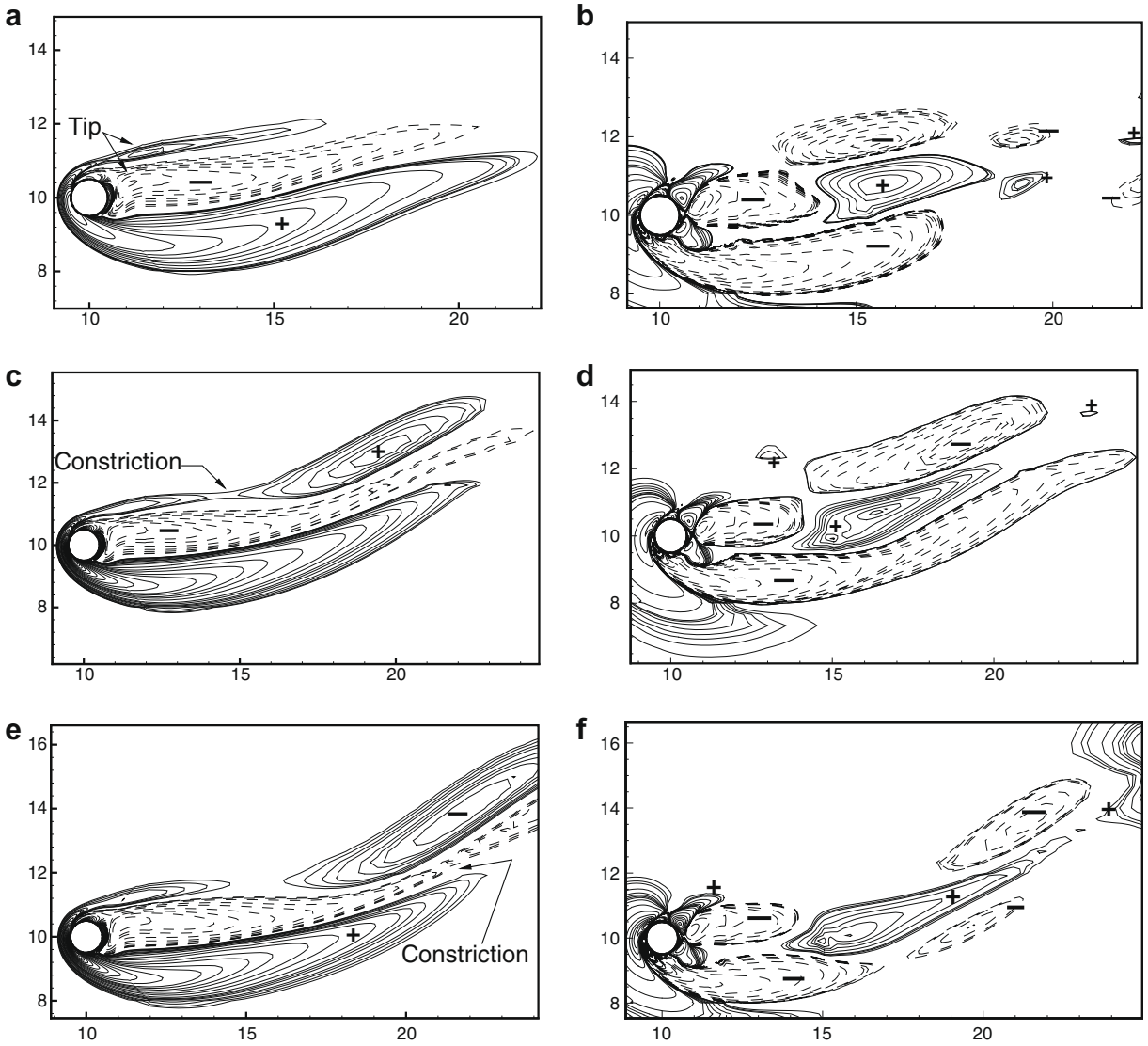

Fig. 15. Instantaneous contours of ω for Re = 45 and Ri = 2.0 at (a) t, (c) $t + \frac{\tau}{3}$, (e) $t + \frac{2\tau}{3}$ (close-up view). Instantaneous contours of γ for Re = 45 and Ri = 2.0 at (a) t, (c) $t + \frac{\tau}{3}$, (e) $t + \frac{2\tau}{3}$ (close-up view).

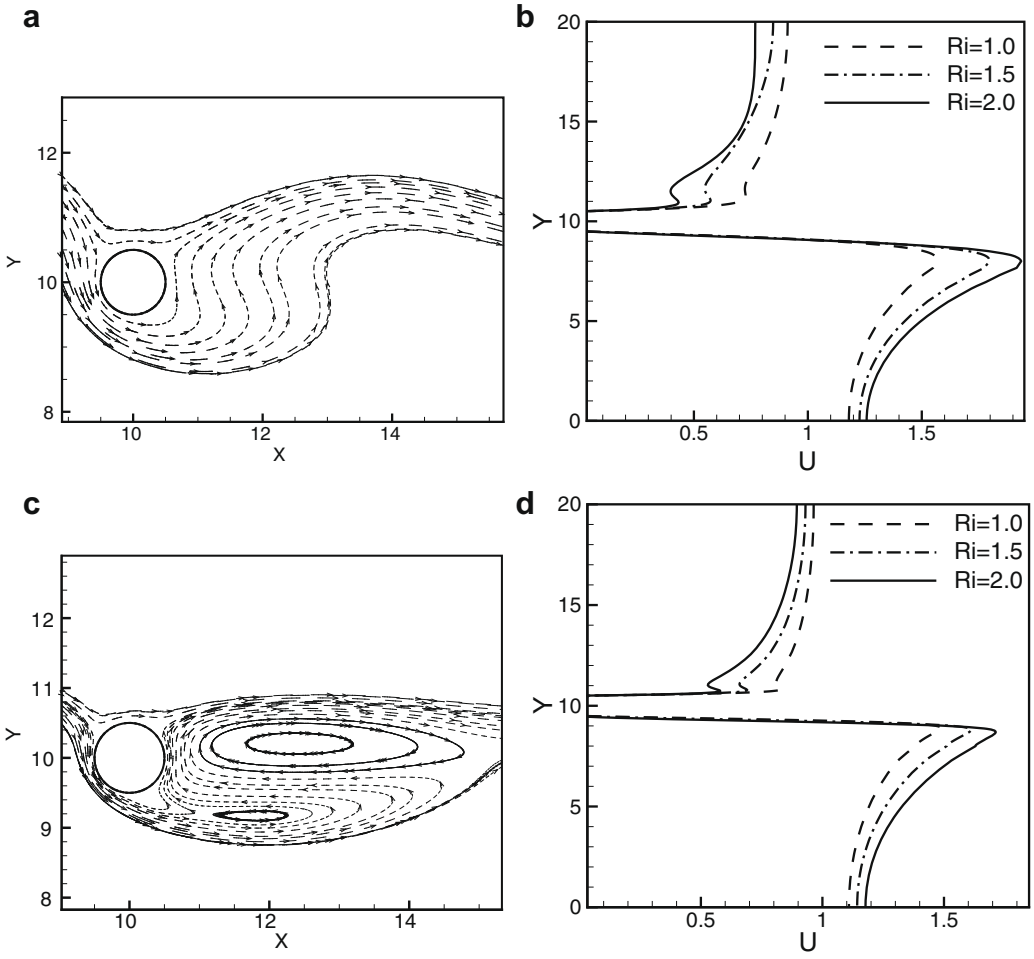

Fig. 16. Streamline pattern close to the cylinder for Re = (a) 10 and (c) 45 at Ri = 2.0 and u-velocity profiles at $x = 10$ for different Ri at Re = (b) 10 and (d) 45.

therms with vorticity is that in the former case only one strand of isotherms connecting with the vicinity of the cylinder is found. The sequence of transportation of thermal energy is shown by the plots of isotherms as shown in Fig. 10(a–d). This process of transportation starts with the stretching of a hot strand of warm fluid, originating in the vicinity of the cylinder [Fig. 10(a)] into the cylinder near wake. A local temperature extreme is found at the tip of the strand. Gradually this extreme develops [Fig. 10(b)] in a confined area and later the strand connecting the area with the cylinder starts to constrict [Fig. 10(c)]. Finally, it is separated out and forms an isolated hot blob which is convected downstream of the cylinder [Fig. 10(d)].

Fig. 11(a–d) show the instantaneous streamlines in a complete vortex shedding period captured at time instants $t, t+\frac{\tau}{4}, t+\frac{2\tau}{4}$ and $t+\frac{3\tau}{4}$.

Generation and advection of a recirculated zone are found during the vortex shedding cycle near the upper boundary of the physical domain (see Fig. 11). The formation and advection process can be explained in the following way. During the vortex shedding cycle, the lower vortex sheds from the upper half of the cylinder shoulder due to the effect of strong superimposed buoyancy. As the Reynolds number is low, buoyancy dominates. Due to the strong buoyant force, the shed vortex reaches the upper boundary of the computational domain. Fig. 12 illustrates that the zone of recirculating streamlines coincides with the shed vortex. Finally, with the advection of that vortex, this recirculating zone also moves out of the domain and the process continues. This recirculating zone is observed only for Re = 10 and Re = 15 at Ri = 2.0.

4.4. Behavior of the wake under superimposed buoyancy at Re = 45

It is found that with increasing Reynolds number the effect of buoyancy on the flow reduces and vortex shedding takes place at a higher Richardson number. For a Reynolds number of 45, a steady wake is found below a Richardson number of 1.985. Fig. 13(a–d) show steady-state solutions for Ri = 1.0. Fig. 14(a–d) show the behavior of wake for Ri = 1.985 at Re = 45. At this Ri, the wake becomes unsteady and vortex shedding is observed.

The formation of the vertical structure for a Reynolds number of 45 at Ri = 2.0 is shown in Fig. 15. The iso-contours of ω and γ are computed at the time instants $t, t+\frac{\tau}{3}$ and $t+\frac{2\tau}{3}$ during the vortex shedding cycle. The formation process is the same as described earlier for Re = 10 [Fig. 9(a–f)].

From Fig. 15(a–f), it is evident that the location of the zone of constriction is larger than that of Re = 10 [Fig. 9(c) and (f)], which is due to the effect of the larger Reynolds number. Here both vortices are shed from the upper half of the cylinder shoulder.

4.5. Flow pattern around the cylinder

The transport of any quantity can be considered along the streamlines when diffusion transport is neglected. The dashed streamlines in Fig. 16(a) and (c) show the net amount of fluid transported from the lower half of the wake into the upper half for Re = 10 and Re = 45 at Ri = 2.0 close to the cylinder. High heating results in an upward drift of the streamlines in the wake zone of the cylinder. The streamlines reveal that a net amount of fluid is

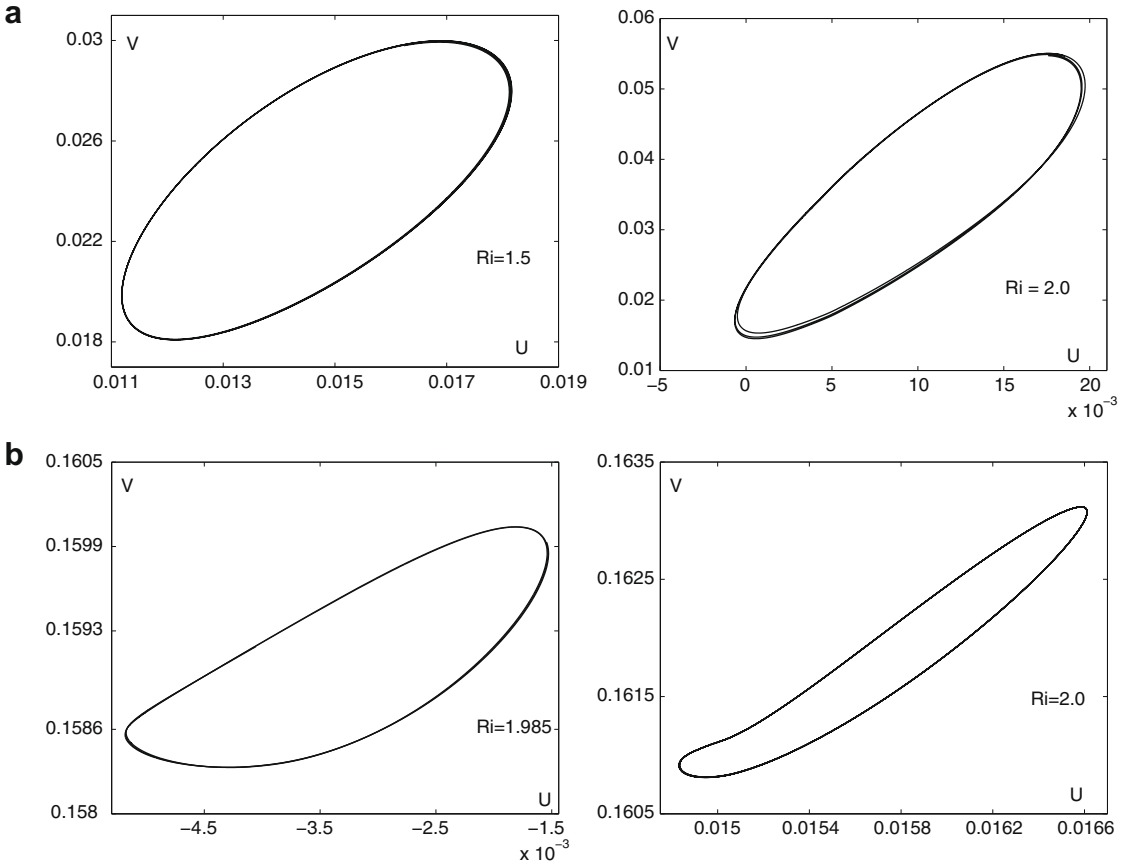

Fig. 17. Phase diagrams for Re = (a) 10 and (b) 45 and various Ri.

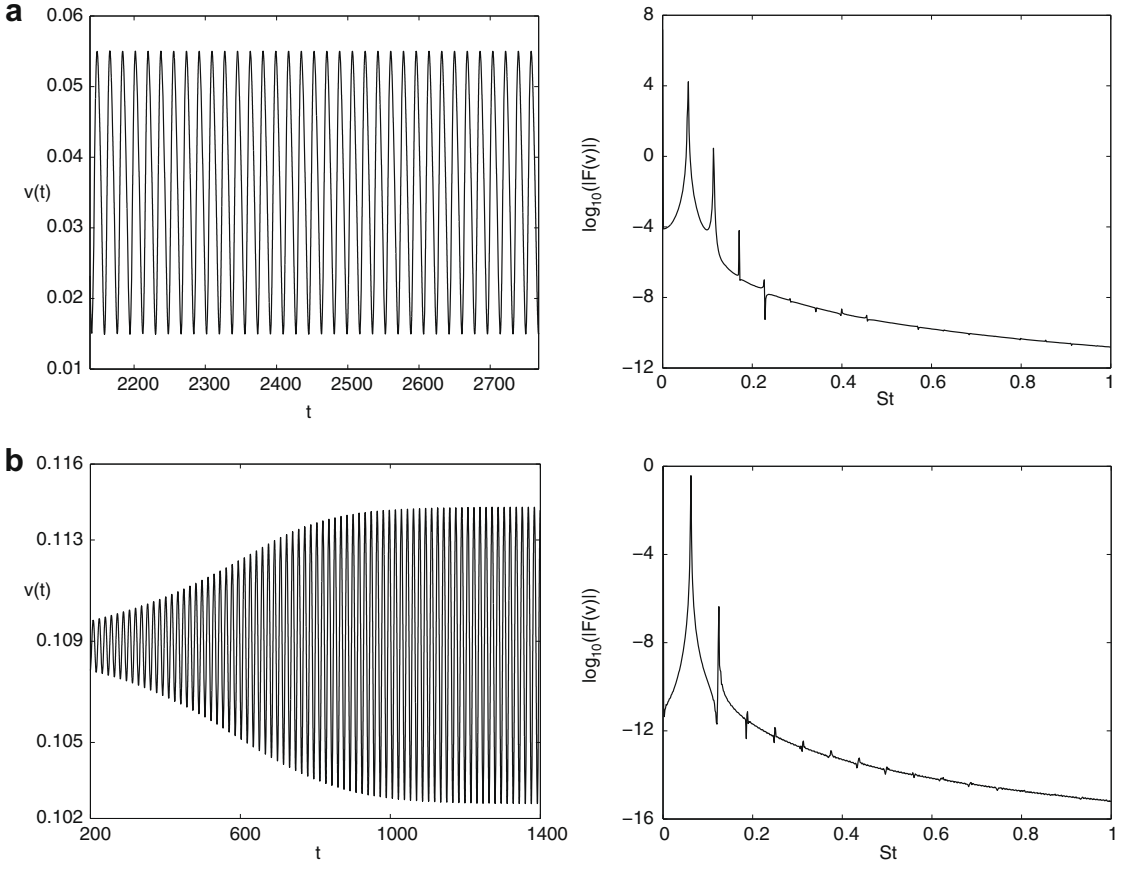

Fig. 18. Transverse velocity signals versus non-dimensional time and fast Fourier transform for Re = (a) 10 and (b) 45 at Ri = 2.0.

transported from the lower half of the wake into the upper half. This fluid transport is depicted by the dashed streamlines. Fluid between the cylinder and these streamlines first moves underneath the cylinder but finally moves up in the upper half of the wake. The mass conservation principle then demands transportation of a large amount of fluid from underneath the cylinder, which is supported by the fact that with increasing Ri, the values of u-velocity underneath the cylinder increases and its percentage increase is more than that in the upper half, as shown in Fig. 16(b) and (d) for Re = 10 and Re = 45, respectively, at x/D = 10.

4.6. Phase diagrams

Fig. 17(a and b) show phase diagrams for different Richardson numbers at Reynolds numbers of 10 and 45, respectively. We have already seen that for the combination of Richardson numbers and Reynolds numbers the vortices are shed into the stream and the flow field becomes periodic. These phase diagrams were constructed by plotting the temporal variation of the streamwise velocity component at a sampling location 5D downstream of the cylinder against the transverse velocity component at the same location. At the sampling point, the transverse velocity component dominates the streamwise velocity component. The phase diagrams clearly indicate the periodic nature of the flow.

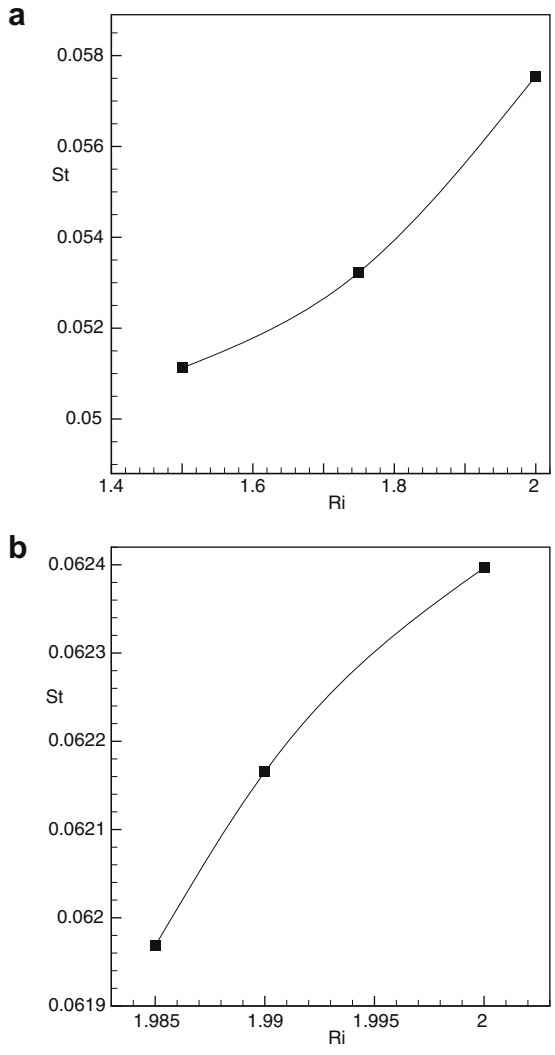

Fig. 19. Variation of Strouhal number with Richardson number for Re = (a) 10 and (b) 45 during vortex shedding.

4.7. Vortex shedding frequency

Periodicity is induced in the flow field due to the vortex shedding phenomenon. The periodicity is characterized by the Strouhal number (St). Strouhal numbers were calculated for Re = 10 and Re = 45 for various Richardson numbers in the shedding regime. Fig. 18(a) and (b) show the transverse velocity signal and its FFT (fast Fourier transform) captured at the sampling location 5D downstream from the center of the cylinder for Re = 10 and Re = 45, respectively, at Ri = 2.0.

Basically transverse velocity signals show the growth of the signal to saturation at that particular sampling location. The corresponding FFTs show the decadic logarithm of the modulus of the Fourier transform of the transverse velocity as a function of Strouhal number. The local peaks of the FFT curve confirm the presence of different harmonics in the velocity signal.

Fig. 19(a and b) show the variation of St for Re = 10 and Re = 45, respectively, for different Ri. The shedding frequency is observed to increase with increase in Ri. The trend of variation of St for Re = 10 is similar to those reported by Patnaik et al. [26].

Fig. 20 shows the variation of Strouhal number as a function of Reynolds number for a fixed Richardson number of 2. It is clear that shedding frequency increases sharply with increase in Reynolds number up to Re = 25 and thereafter it reduces until a Reynolds number of 40. The frequency increases marginally Re = 40.

4.8. Periodic characteristics of separation angle (θ_s) and average Nusselt number ($\overline{Nu_\theta}$)

It is found that during the vortex shedding cycle, the separation angle and the average Nusselt number calculated at the cylinder surface vary at each instant. Fig. 21(a and b) show the variations of separation angle and the average Nusselt numbers at Re = 45 for Ri = 2.0. It is found that the vortex shedding frequency at that particular Ri is same as the frequency of variation of the separation angle and the average Nusselt number for those Reynolds numbers. The trend of variation of the separation angle is similar to that reported by Wu et al. [12]. Wu et al. [12] have shown that the value of θ_s decreases with increasing Reynolds number. However, the variation in θ_s values increases significantly as the Reynolds number increases beyond the critical Reynolds number. In the present study the variation in θ_s is brought about as the Richardson number increases beyond the critical Richardson number.

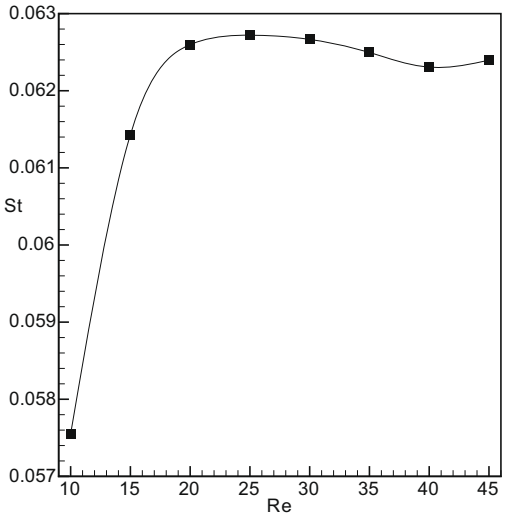

Fig. 20. Variation of Strouhal number with Reynolds number at Ri = 2.0.

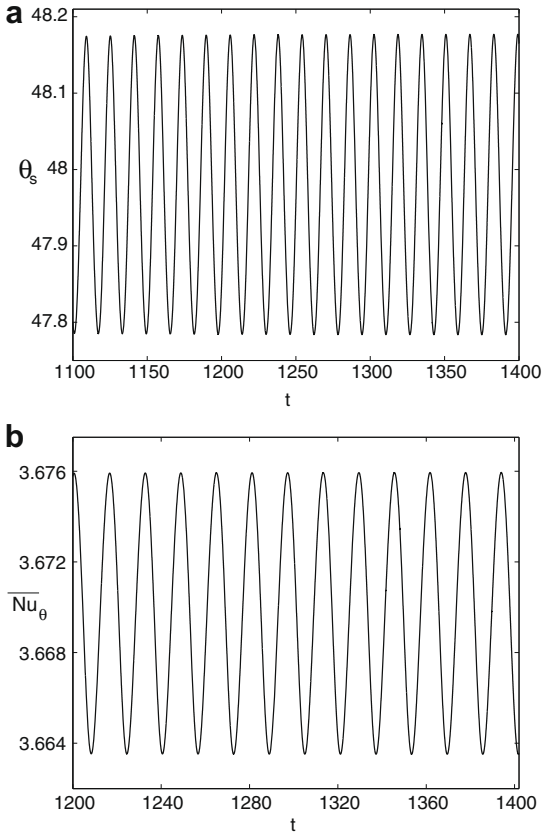

Fig. 21. Variation of (a) separation angle (θ_s) and (b) average Nusselt number ($\overline{Nu_\theta}$) during vortex shedding cycles for Re = 45 and Ri = 2.0.

5. Conclusions

The segregated SUPG-based finite element approach is an efficient numerical tool to solve complex flows with much reduced computational effort. The streamline upwinding minimizes cross-wind diffusion. The consistent Petrov–Galerkin weighted residual formulation proves to be key feature for the success of this method. A numerical investigation was carried out to study the flow and heat transfer behavior past a circular cylinder in the range of Reynolds numbers 10–45 under varying thermal buoyancy. In the absence of thermal buoyancy, the separation angle and the eddy length increase with increasing Reynolds number. The predicted results match well with those available in the literature. During forced convection, the maximum heat transfer occurs at the front stagnation point and decreases to a minimum at the rear stagnation point. The average Nusselt number also increases with increasing Reynolds number and the predicted results are in conformity with well-known experimental observations. This study confirms that the characteristics of the steady wake downstream of a cylinder can be altered by superimposed thermal buoyancy. Under the influence of superimposed thermal buoyancy, the flow becomes unsteady periodic. The thermal buoyancy brings about asymmetry in the wake and induces unsteadiness. Beyond some critical value of Ri for a given Reynolds number, vortex shedding starts. For Re = 10 vortex shedding is observed at Ri = 1.4 and for Re = 45 vortex shedding starts at Ri of 1.985. The vortex shedding cycles were described at Ri = 2.0 with the help of iso-contours of vorticity, ω and a parameter γ that indicates the vorticity accumulation and vortex structure formation. It is also found that the Strouhal number varies with Ri and Re. The separation angle (θ_s) and average Nusselt number ($\overline{Nu_\theta}$) are found to be influenced by the vortex shedding. The separation angle (θ_s) and the average Nusselt number ($\overline{Nu_\theta}$) oscillate with the frequency of the shedding.

Acknowledgement

The authors are indebted to Prof. Dr. Franz Durst of FMP Technology GmbH, Erlangen (Germany) for useful discussions.

References

[1] S. Taneda, Experimental investigation of the wakes behind cylinders and plates at low Reynolds numbers, J. Phys. Soc. Jpn. 11 (1956) 302–307.
[2] M. Coutanceau, R. Bouard, Experimental determination of the main features of the viscous flow in the wake of a circular cylinder in uniform translation. Part 1. Steady flow, J. Fluid Mech. 79 (1977) 231–265.
[3] S.C.R. Dennis, J.D. Hudson, N. Smith, Steady laminar forced convection from a circular cylinder at low Reynolds number, Phys. Fluids 11 (5) (1968) 933–940.
[4] H. Jafroudi, H.T. Yang, Steady laminar forced convection from a circular cylinder, J. Comput. Phys. 65 (1986) 45–56.
[5] C.J. Apelt, M.A. Ledwich, Heat transfer in transient and unsteady flows past a circular cylinder in the range 1 < R < 40, J. Fluid Mech. 95 (4) (1979) 761–777.
[6] P.H. Oosthuizen, S. Madan, The effect of flow direction on combined convective heat transfer from cylinders to air, J. Heat Transfer 93 (1971) 240–242.
[7] H.M. Badr, Laminar combined convection from a horizontal cylinder – parallel and contra flow regimes, Int. J. Heat Mass Transfer 27 (1) (1984) 15–27.
[8] B.S.V. Patnaik, P.A.A. Narayana, K.N. Seetharamu, Finite element simulation of transient laminar flow past circular cylinder and two cylinders in tandem influence of buoyancy, Int. J. Numer. Methods Heat Fluid Flow 10 (6) (2000) 560–580.
[9] S. Singh, G. Biswas, A. Mukhopadhyay, Effect of thermal buoyancy on the flow through a vertical channel with a built-in circular cylinder, Numer. Heat Transfer Part A 34 (1998) 769–789.
[10] G. Biswas, H. Laschefski, N.K. Mitra, M. Fiebig, Numerical investigation of mixed convection heat transfer in a horizontal channel with built-in square cylinder, Numer. Heat Transfer Part A 18 (1990) 173–188.
[11] A.-B. Wang, Z. Travnicek, K.-C. Chia, On the relationship of effective Reynolds number and Strouhal number for the laminar vortex shedding of a heated circular cylinder, Phys. Fluids 12 (6) (2000) 1401–1410.
[12] M.-H. Wu, C.-Y. Wen, R.-H. Yen, M.-C. Weng, A.-B. Wang, Experimental and numerical study of the separation angle for flow around a circular cylinder at low Reynolds number, J. Fluid Mech. 515 (2004) 233–260.
[13] J.-M. Shi, D. Gerlach, M. Breuer, G. Biswas, F. Durst, Heating effect on steady and unsteady horizontal laminar flow of air past a circular cylinder, Phys. Fluids 16 (12) (2004) 4331–4345.
[14] R. Kieft, C.C.M. Rindt, A.A. van Steenhoven, Near-wake effects of heat input on the vortex-shedding mechanism, Int. J. Heat Fluid Flow 28 (2007) 938–947.
[15] P.K. Maji, G. Biswas, Analysis of flow in the spiral casing using a streamline upwinding Petrov–Galerkin method, Int. J. Numer. Methods Eng. 45 (1999) 147–174.
[16] F.H. Harlow, J.E. Welch, Numerical calculation of time-dependent viscous incompressible flow of fluid with free surface, Phys. Fluids 8 (1965) 2182–2188.
[17] A.N. Brooks, T.J.R. Hughes, Streamline upwind Petrov–Galerkin formulations for convection dominated flows with particular emphasis on the incompressible Navier–Stokes equations, Comput. Methods Appl. Mech. Eng. 32 (1982) 199–259.
[18] K. Arul Prakash, G. Biswas, B.V. Rathish Kumar, Thermal hydraulics of the spallation target module of an accelerator driven sub-critical system: a numerical study, Int. J. Heat Mass Transfer 49 (2006) 4633–4652.
[19] N. Senthil Kumar, G. Biswas, A finite element study of the onset of vortex shedding in a flow past two-dimensional circular cylinder, Prog. Comput. Fluid Dyn. 8 (2008) 288–298.
[20] H. Takami, H.B. Keller, Steady two-dimensional viscous flow of an incompressible fluid past a circular cylinder, Phys. Fluids (Suppl. II) (1969) 51–56.
[21] S.C.R. Dennis, G.-Z. Chang, Numerical solutions for steady flow past a circular cylinder at Reynolds numbers up to 100, J. Fluid Mech. 42 (3) (1970) 471–489.
[22] R.B. Green, J.H. Gerrard, Vorticity measurements in the near wake of a circular cylinder at low Reynolds numbers, J. Fluid Mech. 246 (1993) 675–691.
[23] J.H. Gerrard, The mechanics of the formation region of vortices behind bluff bodies, J. Fluid Mech. 25 (1966) 401–413.
[24] R.N. Kieft, C.C.M. Rindt, A.A. Van Steenhoven, G.J.F. van Heijst, On the wake structure behind a heated horizontal cylinder in cross-flow, J. Fluid Mech. 486 (2003) 189–211.
[25] J. Weiss, The dynamics of enstrophy transfer in two-dimensional hydrodynamics, Physica D 48 (1991) 273–294.
[26] B.S.V. Patnaik, P.A.A. Narayana, K.N. Seetharamu, Numerical simulation of vortex shedding past a circular cylinder under the influence of buoyancy, Int. J. Heat Mass Transfer 42 (1999) 3495–3507.